Temperature sensitivity of passive holographic wavelength-division multiplexers–demultiplexers

Xuegong Deng, Dechang An, Feng Zhao, Ray T. Chen, and Victor Villavicencio

We derive a set of concise formulas to characterize the temperature sensitivity of holographic wavelength-division multiplexers–demultiplexers (H-MUX's–H-DMUX's). The normalized parameters such as dispersion abilities, central wavelength shift rate, and variations of insertion loss hold for general grating-based wavelength-division multiplexing–demultiplexing (WDM–WDDM) structures. The results are applicable to both wide-WDM–WDDM and dense ones working in 800-, 1300-, and 1550-nm optical wavelength windows, regardless of whether their input–output ports are single-mode or multimode fibers. Detailed analysis and experiments are carried out on a fully packaged four-channel H-MUX–H-DMUX. The experimental results at temperatures from 25 to 80 °C fit nicely with the theoretical prediction. We conclude that passive grating-based H-MUX's–H-DMUX's are promising for meeting the requirements on temperature sensitivity in optical data communications and telecommunications. Most of the analysis can be applied to other types of Bragg-grating-based WDM–WDDM. © 2000 Optical Society of America

OCIS codes: 060.4230, 060.0060, 050.7330, 060.1810, 050.0050.

1. Introduction

Continuous demands on communication bandwidth and speed have been increasing the need to update current networks. Because the worldwide primary communications media have chosen optical fibers over other materials, fiber-to-the-home is beginning to join the other information technologies that have been changing our lives from almost every aspect, among which wavelength-division multiplexing–demultiplexing (WDM–WDDM) technologies are the key to tomorrow's developments in data, voice, imaging, and video communications.[1–4] In the near future, passive optical networks and corresponding passive devices must be developed to maximize the market volume and to minimize the amortized equipment costs. Passive holographic multiplexers–demultiplexers (H-MUX's–H-DMUX's) have much simpler structures and greater cost effectiveness over other technologies such as arrayed-waveguide gratings[5,6] and micro-optics techniques.[7] In addition, the grating-based MUX's–D-MUX's of optimal structures need no active control in a certain range of ambient temperature. This is one of the key features leading to possible field deployment of a device.

In this paper we analyze the static temperature sensitivity of the passive H-MUX–H-DMUX. The multiplexing–demultiplexing structure under evaluation is applicable to other MUX's–DMUX's with Bragg gratings in homogeneous media.[8–10] In Section 2 the dispersion abilities of these grating-based demultiplexers are generalized with several normalized parameters. Distinctions among the normalized total dispersion abilities (NTDA's), the normalized geometrical dispersion abilities (NGDA's), and the normalized material dispersion abilities (NMDA's) are clearly emphasized. A simple model is used to quantify coupling of diffracted beams from free space to fibers in a linear array. Some issues about optimal designs of these MUX's–DMUX's are mentioned in Section 3. Concise analytical expressions are derived to investigate the temperature sensitivities of passive H-MUX's–H-DMUX's in Section 4. Experimental results of a fully packaged four-channel H-DMUX are carefully analyzed and compared with theoretical predictions. The experiments confirm the theoretical predictions.

X. Deng, D. An, F. Zhao, and R. T. Chen (raychen@uts.cc.utexas.edu) are with the Microelectronics Research Center, Department of Electrical and Computer Engineering, University of Texas, Austin, Texas 78758. V. Villavicencio is with Radiant Research, Inc., 3006 Longhorn Boulevard, Suite 105, Austin, Texas 78758.
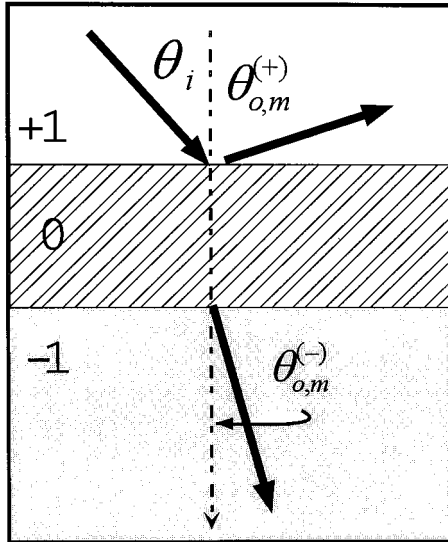
Fig. 1. Diffraction geometry of holographic gratings. The space is divided into three layers, namely, the incident space (or superstrate), the grating layer, and the transmission layer (or substrate), denoted with -1, 0, and $+1$, respectively.

Fig. 2. Normalized material dispersion abilities of BK7 glass and synthetic fused silica.

2. Dispersion Abilities of Passive Holographic Multiplexers–Demultiplexers

The working principle of a H-MUX is the same as that of a H-DMUX. Hence only the properties of demultiplexing structures will be addressed. The key function of these H-MUX's–H-DMUX's is the dispersion of incoming lightwaves. Optical signals of different wavelengths are discriminated and redistributed in the devices. In a general sense, the central part of the H-DMUX consists of a piece of volume holographic grating. Its spatial position in reference to the incoming and the outgoing signals is schematically illustrated in Fig. 1.

The dispersion can be treated accurately as a diffraction process. In Fig. 1 the media are divided into three layers, namely, superstrate, grating, and substrate, which are labeled as regions $+1$, 0, and -1, respectively.[11] Symbols of the three layers' electrical permittivity carry the same superscripts. The thickness of the grating is t. Collimated quasi-plane optical waves are incident from an angle θ_i through the superstrate toward the grating layer. From rigorous coupled-wave theory (RCWT)[11–14] the angular direction of the mth-order harmonics of the reflected (superscript $+$) or transmitted (superscript $-$) wave is

$$\theta_{o,m}^{(\pm)} = \arcsin\left[\frac{k_0\sqrt{\epsilon^{(+)}\mu}\,\sin(\theta_i) + mK}{k_0\sqrt{\epsilon^{(\pm)}\mu}}\right],$$
$$m = 0, \pm 1, \pm 2, \ldots, \tag{1}$$

where $k_0 = 2\pi/\lambda$ is the wave vector in vacuum; $K = 2\pi/\Lambda_x$, and Λ_x is the lateral period of the grating. For dielectric media their permeability μ can be regarded as that of vacuum, and $\sqrt{\epsilon^{(\pm)}\mu} = n^{(\pm)}(\lambda)$ is the refractive index of the material. By differentiating

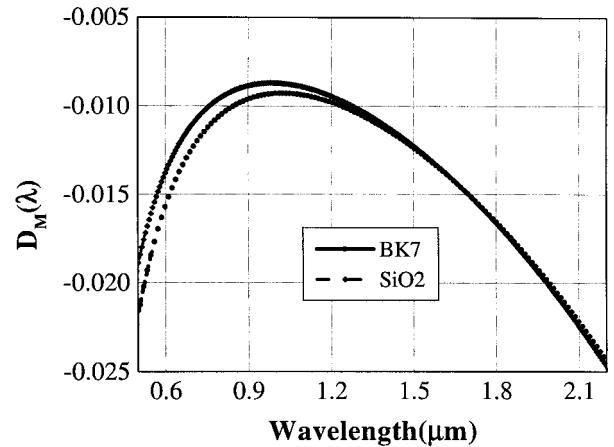Eq. (1) and eliminating mK, $m \neq 0$, we find that the quantity $D_t^{(\pm)}(\lambda) \equiv \lambda\,d\theta_{o,m}^{(\pm)}/d\lambda$, as the NTDA of the grating, can be expressed by

$$D_t^{(\pm)}(\lambda) = \tan[\theta_{o,m}^{(\pm)}][D_M^{(+)}(\lambda) - D_M^{(\pm)}(\lambda)]$$
$$+ D_G^{(\pm)}(\lambda)[1 - D_M^{(+)}(\lambda)], \tag{2}$$

in which we have used the shorthand notation $n_r^{(\pm)}(\lambda) \equiv n^{(+)(\lambda)}/n^{(\pm)}(\lambda)$ for the relative refractive indices, $D_M^{(\pm)}(\lambda)$ and $D_G^{(\pm)}(\lambda)$, to represent the NMDA and the NGDA, respectively, each of which is defined as

$$D_M^{(\pm)}(\lambda) \equiv \frac{\lambda}{n^{(\pm)}(\lambda)}\frac{dn^{(\pm)}(\lambda)}{d\lambda}, \tag{3}$$

$$D_G^{(\pm)}(\lambda) \equiv \frac{\sin[\theta_{o,m}^{(\pm 1)}] - n_r^{(\pm)}(\lambda)\sin(\theta_i)}{\cos[\theta_{o,m}^{(\pm)}]}. \tag{4}$$

When the superstrate and the substrate are made of the same material, Eq. (2) becomes

$$D_t^{(\pm)}(\lambda) = D_G^{(\pm)}(\lambda)[1 - D_M^{(+)}(\lambda)]. \tag{5}$$

Equation (4) has been used as the NTDA for WDM–WDDM applications in many studies,[8–10,15,16] and introduces an error near $-D_M^{(+)}(\lambda)$ that is important for dense WDM–WDDM (D-WDM–D-WDDM) applications. The distinction between NGDA and NTDA is verified in experiments.[17,18]

For most of the optical materials the NMDA is a slowly varying function of wavelength and is usually very small.[19] For example, the NMDA's of BK7 glass and synthetic fused silica (SiO_2) plotted in Fig. 2 are near -0.006 to -0.02 in the wavelength range of $0.5\ \mu m \leq \lambda \leq 2.3\ \mu m$. Therefore, even for the wide WDM–WDDM (W-WDM–W-WDDM) proposed, wavelength variations are no more than 100 nm, and the dispersion corrections coming from the material dispersions as in Eq. (2) could be regarded as constants, i.e.,

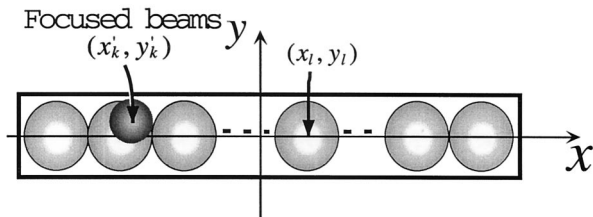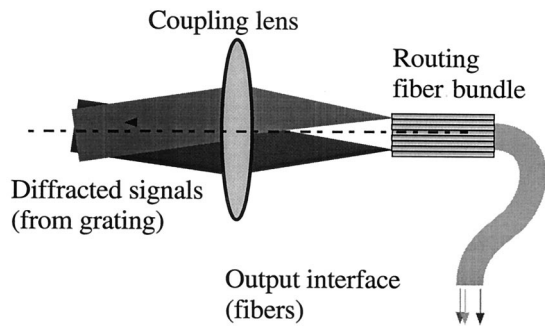$$D_M^{(\pm)}(\lambda) \approx D_M^{(\pm)}(\lambda_c),$$

Fig. 3. Coupling focused beams from free space to *V*-grooved linear fiber array. The fibers are centered at (x_l, y_l), whereas the beams are focused at (x'_k, y'_k), $k, l = 1, 2, 3, \ldots, N_c$.

where λ_c is the central wavelength of the device. The NGDA of gratings, especially those used in D-WDM–D-WDDM, is usually 2 orders of magnitude bigger than those of the NMDA's for most optical materials.[18] A passive H-MUX–H-DMUX must have a sufficiently large yet properly valued NTDA to separate incoming multiwavelength signals and route the signals to different physical outgoing points.[18]

3. Power Losses of the Holographic Wavelength-Division Multiplexer–Demultiplexer at Static Temperatures

The temperature sensitivity of the passive H-MUX–H-DMUX can be characterized with its loss spectra at static temperatures. Dispersed by the grating, optical signals of different wavelengths are routed to individual output ports—usually optical fibers—in a typical H-DMUX. A simple way to accomplish this discrimination of different wavelengths involves focusing the diffracted beams onto linearly spaced fibers permanently fixed in *V* grooves, as shown in Fig. 3. The horizontal positioning accuracy of the fibers in these commercially available arrays can be less than ± 1.0 μm. One advantage of such an arrangement is the elimination of multiple alignments for individual fibers by simultaneous outcoupling of all the channels, which improves the throughput. However, this imposes additional constraints on the MUX–DMUX structures, e.g., trade-offs between good linearity of the outcoupling and high-dispersion abilities, compromises among the dispersion abilities and the bandwidths of the hologram, and contentions between insertion loss and polarization dependence.[18]

Some other important issues must be considered when the beams are coupled to the fiber bundle. One needs to minimize and balance the insertion losses among all the channels. The insertion loss comes from two major sources. One is the diffraction loss, which also determines the passing band of the hologram, and the other is the coupling loss from the focusing lens to the fibers.

A. Bandwidth of the Holographic Wavelength-Division Multiplexer–Demultiplexer

The working wavelength of an N_c-channel WDM–WDDM system is usually located on a grid.[20] For simplicity we symbolically write the wavelengths as

$$\lambda_l = \lambda_c + \left(l - \frac{N_c + 1}{2}\right)\lambda_s, \qquad l = 1, 2, 3, \ldots, N_c, \quad (6)$$

where λ_s is used to denote the wavelength spacing of adjacent channels. With H-MUX's–H-DMUX's, λ_s varying from 2.0 to 30 nm has been experimentally demonstrated.[15,21] This, to our knowledge, is the most flexible DMUX structure reported to date. Therefore the bandwidth of the hologram that constrains the passing band of the H-MUX–H-DMUX should be at least $(N_c - 1)\lambda_s$.

The passing band of the hologram can be found from the diffraction efficiencies of the hologram by use of RCWT's[11–14] or the coupled-mode theory (CMT).[22–24] However, there is a much simpler yet accurate formula being widely adopted to approximate the bandwidth derived by Ludman.[25] Following Ref. 25 we find the single side bandwidth, $\Delta\lambda/\lambda_c$, around the central wavelength λ_c is solely determined by the diffracting geometry and the thickness of the grating so that

$$\frac{\Delta\lambda}{\lambda_c} = \frac{\Lambda_x}{t} \frac{\cos[\theta_{o,-1}^{(\pm)'}]\cos\phi}{\sin(\delta\theta)}, \qquad (7)$$

where ϕ is the slant angle of the grating fringes, $\delta\theta = [\theta'_i - \theta_{0,-1}^{(\pm)'}]/2$, and $\theta_{o,-1}^{(\pm)'}$ is corresponding diffraction angle inside the hologram. One can infer from the expressions of the NTDA in Eq. (5) and this single side bandwidth that there must be a compromise between the dispersion ability and the bandwidth.[15,18,25] To get a high-dispersion ability, the absolute value of $\delta\theta$ as well as ϕ must be much larger than zero, which in turn decreases the bandwidth, and vice versa. However, one may decrease the thickness of the grating in a certain range to increase the bandwidth while not affecting the dispersion ability, which was mentioned in the optimal design of a practical demultiplexer in Ref. 18.

B. Diffraction Efficiencies of the Holograms

The diffraction efficiency of the hologram can be precisely predicted by use of RCWT's.[11–14] For high-diffraction-efficiency holograms, it is also feasible to use the simpler yet accurate the CMT.[22–24] Let Λ be the period of the grating and n_0 the average index of

refraction of the hologram. If the so-called Q factor is

$$Q = 2\pi\lambda_c t / n_0 \Lambda^2 > 10, \qquad (8)$$

then the diffraction occurs in the Bragg regime.[16,23] Hence the analytical expressions for the diffraction efficiency from CMT are as accurate as the numerical results from RCWT. The diffraction efficiencies for s- and p-polarized waves of lossless transmission holograms given by CMT are[16,23]

$$\eta_{\mathscr{J}} = \frac{\sin^2(\nu_{\mathscr{J}}^2 + \zeta^2)^{1/2}}{1 + (\zeta/\nu_{\mathscr{J}})^2}, \qquad \zeta = \vartheta \frac{1}{2C_S}, \qquad \mathscr{J} = s, p, \quad (9)$$

where the normalized parameters

$$\nu_s = \frac{\pi n_1 t}{\lambda (C_R C_S)^{1/2}}, \qquad \nu_p = \nu_s \cos[2(\theta_i' - \phi)], \quad (10)$$

and C_R and C_S are two inclination factors defined by

$$C_R = \cos(\theta_i'), \qquad C_S = \cos(\theta_i') - (K_g/k_0)\cos(\phi). \quad (11)$$

The $\cos[2(\theta_i' - \phi)]$ factor in Eqs. (10) indicates that there always is a phase delay between the s- and the p-polarized waves reaching the maxima of their diffraction efficiencies. To make a polarization-independent H-MUX–H-DMUX, one has to sacrifice some portion of the incident energy if only one piece of the hologram is used.

C. Coupling Losses from Free Space to Fibers

The efficiency of coupling focused beams to fibers is another important factor. It affects not only the insertion loss but also the cross talk among channels of the H-DMUX. In general the numerical aperture of the beam should be no bigger than that of the multimode fiber which is ~0.2. In addition, the wavefront quality of the diffracted beams plays an important role, owing to the phase-sensitive nature of the volume hologram. Diffraction-limited beams are highly desired. For simplicity, we use the energy-in-the-bucket (EIB) model to characterize the coupling from free space to fibers.

The EIB model is straightforward. Assume that the transmission function of the fiber centered at (x_l, y_l) is $W_{F,l}(x, y)$ and that the intensity distribution of the focused beam on the fiber facet is $I_k(x, y)$; then the normalized energy in the fiber (as a bucket collecting light) is

$$E_{k,l} = \frac{\displaystyle\int\int_{-\infty}^{+\infty} W_{F,l}(x, y)I_k(x, y)\mathrm{d}x\mathrm{d}y}{\displaystyle\int\int_{-\infty}^{+\infty} I_k(x, y)\mathrm{d}x\mathrm{d}y},$$

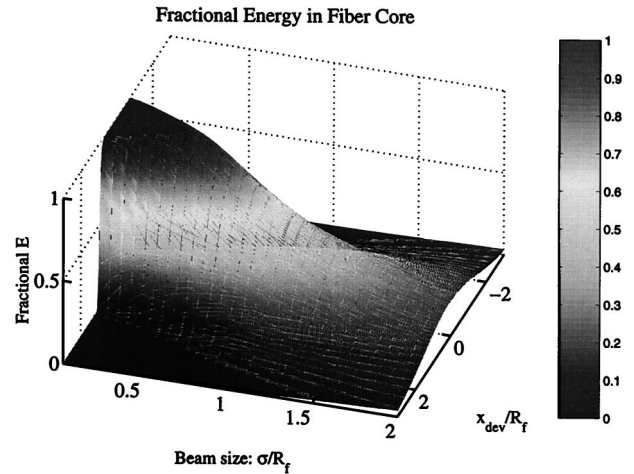$$k, l = 1, 2, 3, \ldots, N_c. \qquad (12)$$

Fig. 4. EIB model of coupling light from free space to fibers. The z axis is the fractional energy in the fiber core while the size of the focused beam is 2σ, the misalignment between the focus center to the fiber center is x_{dev}, and the fiber radius is R_f.

This model is so simple that it neglects the difference on angular launching condition. A three-dimensional plotting of the EIB values for different coupling conditions of the normalized beam width, σ/R_f, and the normalized misalignment distance, x_{dev}/R_f, with R_f the radius of the output fiber, is presented in Fig. 4. Similarly, the cross talk from channel k to channel l can be defined as

$$R_{k,l} = -10 \log_{10}(E_{k,l}/E_{l,l}), \qquad (13)$$

which is a ratio in decibels. The parameters $E_{k,l}$ are simple but sufficient to reveal the issues of interest. Figure 4 can also be used to look up the cross talk.

A good MUX–DMUX certainly needs to balance the loss spectra of all the working channels. For a passive structure this is essentially determined by the aforementioned parameters, such as the dispersion abilities, the linearity of outcoupling, the bandwidth, and coupling losses, and the like. Trade-offs have to be made among these key parameters for an optimal design,[18] which is also reflected in the temperature sensitivity of the device.

4. Temperature Sensitivity of the Holographic Wavelength-Division Multiplexer–Demultiplexer

Only static temperature sensitivity is considered in this study; i.e., there is no temperature gradient across the device. We use two parameters to characterize the temperature sensitivity, namely, the central wavelength shift (CWS) of each individual channel, $\Delta\lambda_{c,l}$, $l = 1, 2, 3, \ldots, N_c$, and the insertion loss variations (ILV's) when the working temperature changes. The CWS is used to indicate the channel stability, because the ILV is a good benchmark of signal strength. For field deployment both CWS's and ILV's should be as small as possible across the working temperature range.

Table 1. Coefficients of Thermal Expansions of the Materials Involved in the H-MUX–H-DMUX[a]

Material	CTE ($\times 10^{-6}$/°C)
BK7	7.1
Si	2.46
SiO_2	0.55
Al	21.0–23.2
Steel	17.3
NOA 61	200–220
DuPont film	~43
Pyrex	3.25

[a]Unless stated otherwise in the text, the data were collected from Ref. 35.

A. Central Wavelength Shift of Individual Channels

For fixed incident and outgoing angles the wavelength shift of each individual channel can be found from the geometry of the DMUX and the grating equation, e.g., Eq. (1). For simplicity we consider only the variations caused by the grating in this section when the working temperature changes. The normalized CWS rate (NCWSR) for each channel is

$$\Gamma_l(T) \equiv \frac{1}{\lambda_{c,l}} \frac{\partial \lambda_{c,l}}{\partial T} = \beta_T + (1-\tau)\gamma^{(+)} + \tau\gamma^{(\pm)},$$

$$l = 1, 2, 3, \ldots, N_c, \qquad m \neq 0, \qquad (14)$$

in which β_T is the coefficient of linear thermal expansion (CTE) of the grating,

$$\beta_T = \frac{1}{\Lambda_x} \frac{\partial \Lambda_x}{\partial T}, \qquad (15)$$

and $\gamma^{(+)}$ and $\gamma^{(-)}$ are thermal coefficients of the index of refraction of the superstrate and the substrate of the grating, respectively,

$$\gamma^{(\pm)} = \frac{1}{n^{(\pm)}} \frac{\partial n^{(\pm)}}{\partial T}. \qquad (16)$$

In Eq. (14) τ is a fractional number that may be negative,

$$\tau = \frac{\sin[\theta_{o,m}^{(\pm)}]}{\sin[\theta_{o,m}^{(\pm)}] - n_r^{(\pm)}\sin(\theta_i)}. \qquad (17)$$

We can infer from Eq. (14) that the CWS of the MUX–DMUX is by and large determined by the thermal properties of the grating materials. It is independent of the wavelength separations among channels. One can choose materials for the grating and its surrounding media to minimize the NCWSR.

For most optical materials, either β_T or $\gamma^{(\pm)}$ are small. The typical value of the CWS's of a H-MUX–H-DMUX working in the air is approximately $\Delta\lambda_{c,l} \approx [\beta_T + \gamma^{(\pm)}]\lambda_c\Delta T$, $\Delta T \equiv T_H - T_L$, across the temperature range from T_L to T_H. For example, $\gamma(\text{air}) = -8.9 \times 10^{-7}$/°C, if the grating is made out of quartz (SiO_2); $T_L = -25$ °C; $T_H = 75$ °C; $\Delta\lambda_{c,l}$ is approximately 2.9×10^{-2}, 4.5×10^{-2}; and 5.3×10^{-2} nm for $\lambda_c = 850$, 1300, and 1555 nm, respectively. These

values are encouraging for both W-WDM and D-WDM applications. The CTE's of several materials are listed in Table 1.

B. Diffraction Efficiency Variations

The diffraction efficiency of the volume hologram changes with the temperature. Starting with Eqs. (9)–(11) and after a lengthy but straightforward derivation, one can easily obtain the following expression for the efficiency variation,

$$\frac{1}{\gamma_\mathcal{J}} \frac{\partial \eta_\mathcal{J}}{\partial T} = \frac{2\cos(\nu_\mathcal{J})}{\sin(\nu_\mathcal{J})} \nu_\mathcal{J} \left\{ \gamma_g + \beta_T \left[1 - \frac{K_g\cos(\phi)}{2k_0 C_S} \right] \right\},$$

$$\mathcal{J} = s, p, \qquad (18)$$

which is valid for Bragg holograms as is the case of interest. As in Eqs. (14), $\gamma_g = \partial n_g/n_g\partial T$ is the thermal coefficient of the index of refraction of the grating layer. When SiO_2 is taken as an example, the typical value of the variation for $T_L = -25$ °C and $T_H = 75$ °C is $\sim 10^{-4}$, which is far too small to be of interest in practice. This is a good indication that there is no bandwidth variation of significance.

C. Insertion Loss Variations

For incidence at constant wavelengths in each channel of a DMUX, the insertion losses depend mainly on the angular deviations of the diffracted beams, as described in Subsection 3.C. From Eqs. (1) and (4), one easily finds

$$\frac{\partial \theta_{o,m}^{(\pm)}}{\partial T} = -\Gamma_l(T) D_G^{(\pm)}(\lambda). \qquad (19)$$

This equation states that the angular shift of the outcoupling signal is proportional to both the NGDA and the NCWSR. For a coupling lens or lens system of effective focal length f in the DMUX, relative spatial shifts on the fiber array facets are

$$\frac{\delta_S}{R_f} \approx \frac{f}{R_f} \frac{\partial \theta_{o,m}^{(\pm)}}{\partial T} \Delta T, \qquad (20)$$

whereas the consequent values of ILV's can be obtained from Eqs. (12) and (13) or looked up from Fig. 4.

The physical meaning of relation (20) is clear. One can rearrange it as

$$\frac{\delta_S}{R_f} \approx -\frac{fD_G^{(\pm)}(\lambda)\lambda_s}{\lambda_c R_f} \frac{\lambda_c\Gamma_l(T)\Delta T}{\lambda_s} = -\frac{s_0}{R_f} \frac{\Delta\lambda}{\lambda_s} \qquad (21)$$

by using Eqs. (6) and (19) and some quantities defined in Section 3. $s_0 \approx fD_G^{(\pm)}(\lambda)\lambda_s/\lambda_c$, $\Delta\lambda = \lambda_c\Gamma_l(T)\Delta T$ is nothing but the CWS of the channel. It is worth noting that the leading factor s_0/R_f in relation (20) clearly states that the bigger the fiber core R_f relative to the fiber spacing s_0, the better the temperature stability of the device for the same CWS. For example, the temperature stability of a 250-μm-spaced multimode fiber array with $2R_f = 62.5$ μm is equivalent to a 40-μm-spaced single-mode fiber ar-
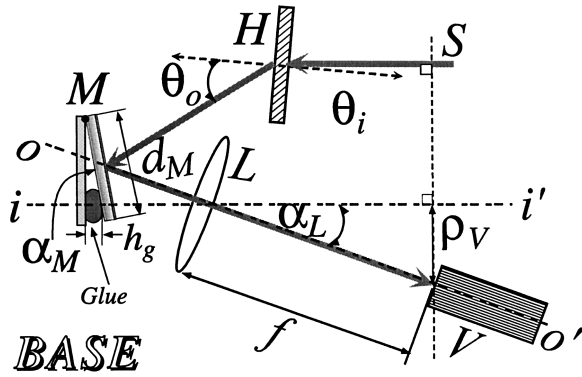
Fig. 5. Schematic top view (not to scale) of the fully packaged four-channel 1 H-DMUX. Both the input (before the collimator S) and the four outputs (at V) are multimode gradient-index fibers with a core size of 62.5 μm. H, hologram; M, mirror; L, coupling lens; V, four-channel fibers in a linear spaced V groove.

ray, given a fiber core size of 10 μm. Through these numbers one can gain a sense of why it is more difficult to maintain the same temperature stability of a single-mode WDDM device with ordinary commercially available fiber arrays that usually have a fiber-to-fiber spacing of more than 100 μm.

5. Experiments on a Four-Channel Holographic Wavelength-Division Demultiplexer

The CWS or the ILV of an optimally designed H-MUX–H-DMUX can be too small for easy direct measurement. Such an experiment demands highly stable light sources and extremely sensitive detections that may not be feasible without specialized equipment. However, one may manifest these effects by using materials with high-value CTE's in the device.

A. Thermal Analysis of a Packaged Device

We built a four-channel H-DMUX. Its structure is illustrated in Fig. 5. The nominal center wavelengths of the device are 750, 780, 810, and 840 nm. In Fig. 5 collimated beams at multiple wavelengths coming from S are demultiplexed by the hologram H. The beams then are reflected by a mirror M toward the coupling lens L which routes each of the four beams around the corresponding center wavelengths to fibers 250 μm linearly in an array V. In the device the hologram is made of the DuPont holographic film HRF600-X001-20.[26–28] The 20-μm-thick film was laminated onto a flat 1-mm-thick BK7 glass substrate, in which holograms were formed. The incident angle $\theta_i = 0$, whereas the diffracted beams deviate near $\theta_{o,m} \approx 0.6917$ (39.63°) in the air. The Q factor of the hologram obtained from Eq. (8) is ~16. Its dispersion ability $D_G(\lambda) \approx -0.8281$. The focal length of the coupling lens is 8.0 mm. Both the input and the output ports are connectorized with multimode gradient-index fibers and ST connectors. All the components are permanently fixed to the aluminum base plate by application of UV-curing epoxy.

We greatly simplify the analysis of the thermal

sensitivity by adopting the results for holograms from Section 4. We need to focus only on the thermal effects of the remaining components in the device. The analysis of the CWS and the ILV can be separated, since the CWS relates only to the relative movements of the components in the horizontal direction, namely, in the signal plane $S \rightarrow H \rightarrow M \rightarrow L \rightarrow V$, whereas the major contribution to the ILV's comes from the misalignment in the vertical direction when a flat wideband white-light source is used as input to the device.

In Fig. 6 the mirror M moves relative to the backing plate when the temperature of the device changes, since the CTE of the UV-cured glue (Norland NOA 61) behind the mirror is heavily mismatched with that of the aluminium backing plate and the base. The change in the angular position is

$$\Delta\alpha_M = \alpha_M(T_H) - \alpha_M(T_L) \approx \alpha_M(T_L)\left(\beta_g - \frac{\beta_B + \beta_M}{2}\right)\Delta T,$$

$$\alpha_M \ll 1, \tag{22}$$

where $\alpha_M(T_L) \approx h_g/d_M$ is the tilt angle of the mirror at temperature T_L, the thickness of the glue $h_g(25\ °C) \approx 1.52$ mm, and the diameter of the mirror $d_M(25\ °C) = 12.5$ mm; β_g, β_B, and β_M are the CTE's of the glue, the backing aluminum plate, and the mirror (Pyrex), respectively. However, the movement of the mirror is determined mainly by the backing plate and the glue, since $\beta_g \gg \beta_B \gg \beta_M$. The net angular movement of the demultiplexed beams is given by

$$\Delta\theta_o^{(\pm)} = \Delta\theta_{o,m}^{(\pm)} - 2\Delta\alpha_M. \tag{23}$$

The minus sign in the above equation is added, because the movement caused by the hologram, $\Delta\theta_{o,m}^{(\pm)}$, is opposite to the rotation of the beams by the mirror during thermal expansion. Therefore the nominal NCWSR $\Gamma_l^{(n)}(T)$ satisfies

$$\Delta\theta_o^{(\pm)} \equiv \frac{\mathrm{d}\theta_{o,m}^{(\pm)}}{\mathrm{d}T}\Delta T = -\Gamma_l^{(n)}(T)D_G^{(\pm)}(\lambda)\Delta T$$

$$= -\left[\Gamma_l(T) + \frac{\alpha_M(T_L)(2\beta_g - \beta_B - \beta_M)}{D_G^{(\pm)}(\lambda)}\right]D_G^{(\pm)}(\lambda)\Delta T,$$

i.e.,

$$\Gamma_l^{(n)}(T) \equiv \frac{1}{\lambda_{c,l}}\frac{\mathrm{d}\lambda_{c,l}}{\mathrm{d}T} = \Gamma_l(T) + \frac{\alpha_M(T_L)(2\beta_g - \beta_B - \beta_M)}{D_G^{(\pm)}(\lambda)}. \tag{24}$$

The misalignment among the optical components in the vertical direction is summarized in Fig. 6. It is obvious that the relative translating movements between the diffracted beams from H and the mirror M has negligible effects on the coupling of the beams to the fibers in V when the temperature changes. However, there may exist residual angular misalignment from the packaging of the device, which is designated by a parameter θ_v for the tilt of the mirror as illustrated above the mirror in Fig. 6. Note that θ_v should be taken as a constant when the temperature
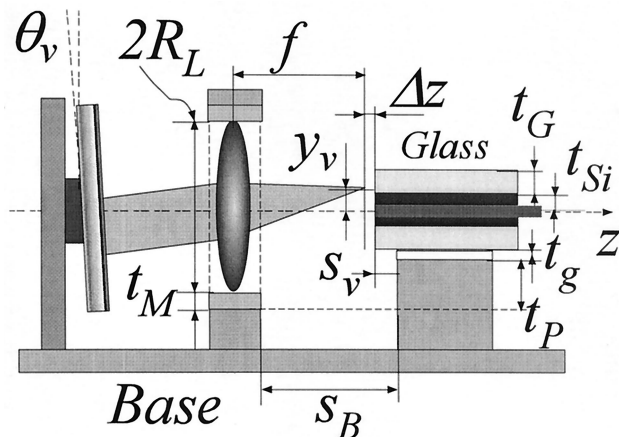
Fig. 6. Schematic side view (not to the scale) of the fully packaged four-channel H-DMUX. The details of the dimensions and the materials of the components are listed in Tables 1 and 2.

changes. The lens L of radius R_L inside a steel mount of thickness t_M is fixed onto an aluminum cell. The drifting of the focused beams relative to the fibers in the V groove in this vertical plane is determined solely by the difference of thermal expansion among the components whose dimensions are summarized in Table 2. The thermal shift rate of the focal length is given by[29]

$$\alpha_f \equiv \frac{1}{f}\frac{df}{dT} = \beta_{\text{glass}} - \frac{1}{n_{\text{glass}} - n_{\text{air}}}\left(\frac{dn_{\text{glass}}}{dT} - n_{\text{glass}}\frac{dn_{\text{air}}}{dT}\right).$$
(25)

Therefore the net displacement of the focused spots relative to the fibers are

$$\Delta y = y_v + \{[\beta(\text{BK7})R_L + \beta(\text{steel})t_M] - [\beta(\text{Al})t_P + \beta(\text{NO A61})t_g + \beta(\text{BK7})t_G + \beta(\text{Si})t_{\text{Si}}]\}\Delta T,$$
(26)

$$\Delta z = [f\alpha_f - \beta(\text{Al})s_B + \beta(V)s_v]\Delta T,$$
(27)

where $\beta(V)$ stands for the CTE of the V groove along the z axis.

One difficulty of predicting the thermal performance of the H-DMUX–H-DEMUX is that we lack sufficient data for the hologram. The CTE's of the components consisting of inhomogeneous materials or more than one kind of material (e.g., the V groove)

Table 2. Dimensions of the Components Illustrated in Figs. 5 and 6 as well as the Materials Involved

Component	Material	Dimensions (mm)
Lens	BK7	$R_L = 4.97$
Lens mount	Steel	$t_M = 0.745$
Base	Al	$S_B = 7.18$
		$t_P = 2.25$
V groove	Si/BK7	$t_{\text{Si}} = 0.549$
		$t_G = 1.00$
Glue	NOA 61	$t_g = 0.152$

are not available. The following parameters have to be estimated with reasonably good accuracy:

1. β_T, the value of the CTE of the hologram. The thermal behavior of the DuPont holographic film we used is by and large confined by the thermal-mechanical properties of the supporting layer (e.g., the Mayer or polyvinyl chloride cover and the BK7-glass substrate). However, the inconsistency of the properties of the polymeric materials makes the estimation difficult.[30] The photopolymer shrinks as much as 5% during the formation of the hologram and tends to stablize after heat treatment.[31] Other studies indicate that the value of the CTE is much larger than that of Mylar.[30] We extracted the CTE of Mylar from Ref. 30, $\beta(\text{Mylar}) \approx 4.3 \times 10^{-5}/°C$, $T = -50 \sim 100 °C$. Meanwhile, the typical CTE value of polymeric materials is approximately $10^{-4}/°C$ (e.g., for polyvinyl chloride, $\beta = 4.7 \times 10^{-4}/°C$),[32] which is far too big compared with the BK7-glass substrate we used to hold the hologram. The real CTE for a thin hologram should approximate that of the substrate, whereas very thick ones should retain the property of the film, since the constraints from the substrate become relatively weak. The dimension of the hologram inside our device is approximately 1.0 cm $\times$ 1.0 cm $\times$ 20 μm. The CTE's of BK7 glass and Mylar are substituted into Eq. (24) as boundaries in our prediction. Despite the complication of the properties of the material, holograms made from the Du-Pont film were reported to be capable of withstanding extreme temperatures ($-55 °C$ to $+125 °C$), heavy relative humidity, and accelerated thermal cycling,[33] which could possibly make the film an excellent candidate for grating materials in optical communications.

2. $\beta(\text{NO A61})$, the CTE of the NOA 61 glue. It has a maximum value of $\sim220 \times 10^{-6}/°C$ at room temperature and decreases slowly to approximately $200 \times 10^{-6}/°C$ at 200 °C. Toward the negative end of the temperature limits (-150 to $+125 °C$) that the glue can withstand, this value decrease sharply to approximately $80 \times 10^{-6}/°C$ at $-50 °C$. An average value $\beta(\text{NO A61}) = 210 \times 10^{-6}/°C$ is taken in our calculation, since the temperature in our experiments is controlled from 25 to 80 °C.

3. $\beta(V)$, the CTE of the V groove along the optical axis. The fibers are sandwiched between two pieces of silicon V grooves, each of which is t_{Si} thick. On each side of the top and the bottom of the V grooves, one piece of BK7 glass of thickness t_G is glued to the silicon serving as a protection layer. This inhomogeneous structure results in a CTE different from that of any individual material inside the V groove. Fortunately, the values of the CTE's of silicon and BK7 are close. They are almost an order of magnitude less than that of the aluminum base plate. Hence the concrete value of $\beta(V)$, taking either $\beta(\text{BK7})$ or $\beta(\text{Si})$, has negligible effect on Δz in Eq. (27).

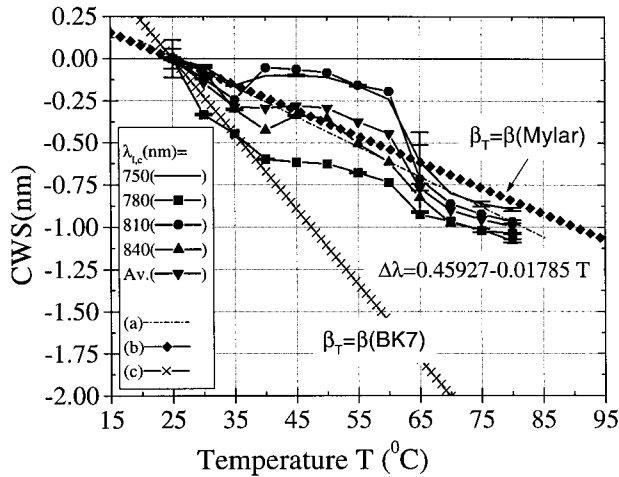When we substitute the parameters in Eqs. (24), (26), and (27) with the values in Tables 1 and 2, the

Fig. 7. CWS's of the fully packaged H-MUX–H-DMUX when working temperature changes. The temperature of device is electronially controlled with an accuracy of ±1 °C from 25 to 80 °C at a 5 °C step. (a) Linear fitting of the average CWS's of the four channels; the slope is -1.785×10^{-2} nm/°C. (b) Boundary of the CWS with the CTE of the Mylar (on top of the hologram) for the hologram. (c) Boundary of the CWS with the CTE of the BK7 glass for the hologram.

Fig. 8. ILV's versus the working temperatures. The temperature of the device is electronially controlled with an accuracy of ±1 °C with an accuracy of ±1 °C from 25 to 80 °C at a 5 °C step.

net NCWSR is bounded by $\Gamma_l^{(n)}(T) = -5.61 \times 10^{-5}$/°C [for $\beta_T = \beta$(BK7)] and -1.93×10^{-5}/°C [for $\beta_T = \beta$(Mylar)]. The misalignment in the vertical plane, which is directly related to the ILV's, are $\Delta y = [y_v - 4.327 \times 10^{-2}\Delta T$ (μm), $\Delta z = -0.138\Delta T$(μm)]. The residual misalignment $y_v = f\theta_v$ is potentially small, which may not be observed when the temperature changes for an optimally aligned device.

B. Comparison with the Experiments

A stable white-light source, whose output power varies less than ±0.05 dB during 1 h in the wavelength range 400–1800 nm, was connected to input fiber of the packaged device. The transmission spectra of the device were obtained by use of an Ando AQ 6312B optical spectrum analyzer (OSA). The wavelength resolution of the OSA is limited to 0.1 nm. The temperature of the device was electronically stabilized with an accuracy of ±1 °C from 25 to 80 °C at a 5 °C step. Each trace of the transmission spectrum was averaged over ten times, and four sets of data were collected for the same channel at the preset temperatures to further average out the fluctuations from the light source and the measurements.

We extracted the CWS's and the ILV's for all the channels from the loss spectrum data by using some data processing techniques outlined in Appendix A. The CWS's and the ILV's are presented in Figs. 7 and 8, respectively. A linear fitting analysis is applied to the average of the CWS data from all channels, resulting a CWS slope $d\lambda/dT = \Gamma^{(\text{expr})}\lambda_c = -1.785 \times 10^{-2}$nm/°C, i.e., $\Gamma^{(\text{expr})} = -2.25 \times 10^{-5}$/°C, which is close to the value confined by the predicted $\Gamma_l^{(n)}(T)$ boundaries. For a H-MUX–H-DMUX of optimized strutures, for example, decreasing mismatches among the CTE's of the components, the values of
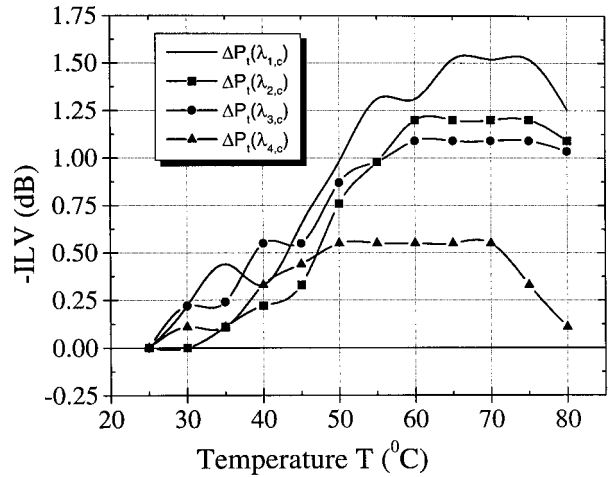
CWS and ILV could be too small for convenient direct measurement in our lab. For example, if the thickness of the glue behind the mirror $h_g = 1.08$ mm, the net NCWSR would be approximately zero. A CWS rate of approximately 8.7×10^{-4} nm/°C was reported for another H-MUX–H-DMUX.[18]

A comparison among the curves in Figs. 7 and 8 confirms our analysis in Subsection 5.A. No associated relation can be found between the CWS and the ILV. Therefore the separation of the movements in the optical axis plane and the perpendicular plane is valid. Some information from Fig. 8 can be useful for evaluating the packaging of the device. All the transmission of the four channels increases with temperature starting from room temperature until ~60 °C. Therefore the insertion loss of the device decreases when temperature increases. Evidence of performance improvement is that there is residual misalignment after the packaging of the device, i.e., $\theta_v \neq 0$. In addition, the difference among the variation rates of the transmission change indicates that the residual misalignment is the relative rotation among the plane of fibers and the focused beam spots. The peaks where the insertion loss becomes the least indicates the correct vertical position of that channel. The channels are better aligned at temperatures near $T_l^* = 69.0, 70.7, 69.3$, and 57.5 °C for $l = 1, 2, 3$, and 4, namely, at wavelengths centered at 750, 780, 810, and 840 nm, respectively. Also, the big difference between $T_l^* \approx 70$ °C ($l = 1, 2, 3$) and the final one $T_4^* = 57.5$ °C suggests that the inital alignment be optimized with respect to the final channel instead of the desired balancing among all four channels. The ILV's of the best aligned channel, i.e., the final one, is also the least (~0.55 dB). There is no noticeable change in its ILV at temperatures from 50 to 70 °C. Similar phenomina exist for the other channels, except that the applicable temperatures varies from channel to channel. The smallest range occurs at the first channel in which the insertion loss is the

worst, indicating the biggest residual misaligment among all the channels. The listed facts are self-consistently cross checked with one another and verify our analysis. These experiments and theoretical predictions suggest that an optimized passive H-MUX–H-DMUX has sufficient thermal stability.

C. Discussions

Temperature sensitivity is one important issue for practical deployment of MUX's–DMUX's. It is of great benefit to the development of the next generation of optical networks if a H-MUX–H-DMUX functions in a reasonable ambient temperature range without any active control mechnism. In our study several normalized parameters, namely, the normalized dispersion abilities, the CWS rate, and the ILV's, are used to summarize the temperature sensitivity of passive H-MUX's–H-DMUX's. The NTDA, NGDA, and NMDA have different effects in the device and are clearly distinguished in our study.

The analysis is based on simple models. However, its validity is not limited to the device under study. The derivations summarized by the normalized parameters hold for or can be adapted to all grating-based devices. The normalization of those parameters also unifies the study of devices working in all three optical wavelength windows, namely, 850, 1300, and 1550 nm. The corresponding thermal sensitivity parameters for a single-mode system is also mentioned in Subsection 4.C. Despite the complicated nonlinearity of the material behaviors involved, the theorectical prediction with the simple models indicates that it is hopeful to eliminate active temperature controls from H-MUX's–H-DMUX's through optimal material selection.

Experiments on a fully packaged H-DMUX are favorably compared with the theorectical prediction. The maximum CWS in this device is ∼1.2 nm at temperatures from 25 to 80 °C, whereas the ILV is 0.55–1.5 dB. The 1.5-dB ILV is a little big, owing to the residual misalignment. In addition, using the multimode fiber array not only greatly eases the alignment of the optics; recent developments in multimode fibers have boosted the transmission speed to 10 Gbit/s over 600 m with 850-nm VCSEL's,[34] whereas the Institute of Electrical and Electronics Engineers is dedicated to developing gigabit ethenet and 10-Gbit ethernet applications. Therefore the widely deployed multimode technologies will continue to evolve and play important roles in data communications.

Although the device under test is a multimode WDM–WDDM device, the analysis still holds for both multimode and single-mode D-WDM–D-WDDM devices, owing to the normalization of the parameters. It is reasonable to anticipate development of completely passive H-MUX's–H-DMUX's with sufficiently low temperature sensitivity.

6. Conclusions

We derived a set of concise formulas to characterize the temperature sensitivity of holographic wavelength-division multiplexers and demultiplexers (H-MUX's–H-DMUX's). The key parameters in the analysis are normalized and make the analysis of a vast variety of WDM–WDDM devices unified within one simple model. The formulas are applicable to both holographic wide WDM–WDDM devices and dense ones, regardless of whether the input–output coupling ports are multimode or single-mode fibers. In addition, this research can be easily extended to Bragg-grating-based structures without difficulty. Most of the formulas, except those for the diffraction efficiencies, are based on the rigorous coupled-wave theories (RCWT's).

Experiments on a fully packaged four-channel H-DMUX directly confirmed our model and analysis when the properties of the materials were involved in the packaging of the device. Many useful conclusions can be drawn from the experimental data on thermal sensitivity. For example, one can use the data to trace the residual misalignment that otherwise is impossible or difficult to measure. For the 20-μm-thick DuPont hologram lamenated onto a piece of 1 cm × 1 cm × 1 mm BK7 glass, the thermal-mechanical behavior in our experiments is determined mainly by the cover sheet of the hologram (Mylar). The normalized central wavelength shift rate (NCWSR) from our experiments fits nicely with the prediction with the property parameters of Mylar. The average CWS over four channels at a rate of -1.785×10^{-2} nm/°C was measured at temperatures from 25 to 80 °C. We suggest that a slight change in the geometry of the device used in our study could result in a much lower CWS rate. Our analysis and experiments indicate that these devices can work stably with temperature ranging from 25 to 80 °C. With careful material selection and optimal designs, passive H-WDM's–H-WDDM's would likely meet the requirements of temperature sensitivity for field deployment in data communications and telecommunications. Other experiments on some single-mode fiber-based WDM–WDDM devices are favorably consistent with these analyses, which we hope to report on soon in a seperate publication.

Appendix A: Data Processing of the Experiments

The CWS or the ILV of an optimally designed MUX–DMUX demands highly stable light sources and extremely sensitive detection that may not be feasible without specialized equipment. In our lab the resolution of the OSA (Ando AQ 6312B OSA) is limited to no better than 0.1 nm. The raw reading from this OSA is certainly not suitable for precise analysis. However, one may improve on the accuracy by taking account of some transmission properties of the grating-based passive MUX's–DMUX's (the loss spectra). One may notice that the coupling efficiencies in Fig. 4 are symmetrical about the amount of misalignment.

Let the input spectrum power density (SPD) of the device be $P_i(\lambda)$ and the transmitted SPD be $P_t(\lambda)$ in the wavelength window $\lambda \in [\lambda_c - \lambda_W/2, \lambda_c + \lambda_W/2]$, and their corresponding readings from the OSA be

$P_i^{(r)}$ and $P_o^{(r)}(\lambda)$, respectively; the transmission spectrum of the channel is

$$P_t(\lambda) = P_o(\lambda)/P_i(\lambda) \approx P_t^{(r)}(\lambda) = P_o^{(r)}(\lambda)/P_i^{(r)}(\lambda),$$

$$\delta\lambda \ll \lambda_{\mathrm{BW}} \ll \lambda_W,$$

where $\delta\lambda$ is the measurement resolution, and λ_{BW} is the passing bandwidth (for example, 3-dB point) of the channel. Assume that the input source is a stable flat wideband spectrum (as in our experiments), and the underlying measurement can be modeled as a filtering process,

$$P_t^{(r)}(\lambda) = P_t(\lambda) * h(\lambda),$$

where $*$ is the convolution operation and $h(\lambda)$ is the narrow-band filter function of the OSA. The support of $h(\lambda)$ is $\sim\delta\lambda$. It is obvious that the first moment (mean) of $P_t^{(r)}(\lambda)$

$$\langle\lambda\rangle = \frac{\int \lambda P_t^{(r)}(\lambda)\mathrm{d}\lambda}{\int P_t^{(r)}(\lambda)\mathrm{d}\lambda} = \frac{\mathscr{P}_t(\nu)'}{\mathscr{P}_t(\nu)}\bigg|_{\nu=0} + \frac{\mathscr{H}(\nu)'}{\mathscr{H}(\nu)}\bigg|_{\nu=0},$$

where $\mathscr{P}_t(\nu)$ and $\mathscr{P}_t(\nu)'$ are the Fourier transform of $P_t^{(r)}$ and the first-order differentiation of $\mathscr{P}_t^{(r)}(\nu)$, respectively. The same is true for $\mathscr{H}(\nu)$ and $\mathscr{H}(\nu)'$ for h. The second term is zero when h is symmetric about λ.

In practice the profiles of P_t should be as accurate as possible. We employed an average ten times for each trace at high sensitivity. Then the test was repeated for four groups, each of which was performed at least 5 min after the previous one. The results were further averaged. Both the mean λ_c^* and the standard deviation were recorded. The fluctuation of the SPD of the light source is less than 0.05 dB during 1 h. The maximum sample point from the OSA is 1001, $\lambda_W = 10$ nm, $\delta\lambda = 0.1$ nm, and the parameter λ_c was obtained by a profile analysis that in principle is the same as outlined here. The results were calibrated and cross verified with another high-resolution OSA (Ando AQ 6317, borrowed from Radiant Research Inc.) with $\delta\lambda = 0.01$ nm. This technique works well for the smooth symmetric loss spectrum that is typical for passive H-MUX's–H-DMUX's. It improves the accuracy of locating the central wavelength over the raw data reading from the OSA.

References and Notes

1. P. Green, "Optical networking has arrived," IEEE Commun. Mag. **36,** 38 (1998).
2. J. P. Ryan, "WDM: North American deployment trends," IEEE Commun. Mag. **36,** 40–44 (1998).
3. C. DeCusatis, "Optical data communication: fundamentals and future directions," Opt. Eng. **37,** 3082–3099 (1998).
4. R. K. Butler and D. R. Polson, "Wave-division multiplexing in the Sprint long distance network," IEEE Commun. Mag. **36,** 52–55 (1998).
5. E. Pawlowski, M. Ferstl, H. Hellmich, B. Kuhlow, C. Warmuth, and J. R. Salgueiro, "Fabrication of a multichannel wavelength-division multiplexing-passive optical net demultiplexer with arrayed-waveguide gratings and diffractive optical elements," Appl. Opt. **38,** 3039–3045 (1999).
6. H. Takahashi, S. Suzuki, K. Kato, and I. Nishi, "Arrayed-waveguide grating for wavelength division multi-/demultiplexer with nanometer resolution," Electron. Lett. **26,** 87–88 (1990).
7. D. Intani, T. Baba, and K. Iga, "Simple optical wavelength-division multiplexer component that uses the lateral focusing scheme of a planar microlens," Appl. Opt. **33,** 3405–3408 (1994).
8. Y. T. Huang, D. C. Su, and Y. K. Tsai, "Wavelength-division-multiplexing and demultiplexing by using a substrate-mode grating pair," Opt. Lett. **17,** 1629–1631 (1992).
9. J.-T. Chang, D.-C. Su, and Y.-T. Huang, "Substrate-mode holographic polarization-division multi/demultiplexer for optical communications," Appl. Opt. **33,** 8143–8145 (1994).
10. J. Liu and R. T. Chen, "Path-reversed substrate-guided-wave optical interconnects for wavelength-division demultiplexing," Appl. Opt. **38,** 3046–3052 (1999).
11. L. Li, "Multilayer modal method for diffraction gratings of arbitrary profile, depth, and permittivity," J. Opt. Soc. Am. A **10,** 2581–2591 (1993).
12. L. Li, "Formulation and comparison of two recursive matrix algorithms for modeling layered diffraction gratings," J. Opt. Soc. Am. A **13,** 1024–1035 (1996).
13. M. G. Moharam, E. B. Grann, D. A. Pommet, and T. K. Gaylord, "Formulation for stable and efficient implementation of the rigorous coupled-wave analysis of binary gratings," J. Opt. Soc. Am. A **12,** 1068–1076 (1995).
14. M. G. Moharam, D. A. Pommet, E. B. Grann, and T. K. Gaylord, "Stable implementation of the rigorous coupled-wave analysis for surface-relief gratings: enhanced transmittance matrix approach," J. Opt. Soc. Am. A **12,** 1077–1086 (1995).
15. R. T. Chen, J. Liu, and X. Deng, "Multimode-fiber-compatible WDM/WDDM with an ultra-large wavelength range," in *Wavelength Division Multiplexing*, R. T. Chen and L. S. Lome, eds., Vol. CR71 of SPIE Critical Reviews of Optical Science and Technology (Society of Photo-Optical Instrumentation Engineers, Bellingham, Wash. 1999), pp. 50–71.
16. R. R. A. Syms, *Practical Volume Holography* (Clarendon, Oxford, 1990).
17. X. Deng, F. Zhao, Z. Fu, J. Zou, J. Qiao, G. Kim, and R. T. Chen, "Linearity of volume hologram out-coupling for wavelength-division demultiplexing," in *WDM and Photonic Switching Devices for Network Applications*, R. T. Chen and G. F. Lipscomb, eds., Proc. SPIE **3949,** 109–119 (2000).
18. X. Deng, F. Zhao, and R. T. Chen, "Optimal design of substrate-mode volume holographic wavelength division demultiplexers," in *WDM and Photonic Switching Devices for*

Network Applications, R. T. Chen and G. F. Lipscomb, eds., Proc. SPIE **3949,** 120–136 (2000).

19. *Optical Glass Catalog* (Schott Glass Technologies, Inc., 1996), http://www.schottglasstech.com/.

20. For a WDM–WDDM system in the 1.55-μm-wavelength window its channel is usually located on an equal-spaced frequency grid such as the International Telecommunication Union standards in telecommunications. However, it is preferable to deal with wavelengths rather than frequencies in optics. For simplicity we ignore the slight nonlinearity of the correspondence between wavelength grid and frequency grid (especially for D-WDM–D-WDDM applications).

21. C. C. Zhou, S. Sutton, R. T. Chen, B. V. Hunter, and P. Dempewolf, "Four channel multimode wavelength division, multiplexer and demultiplexer based on photopolymer volume holographic gratings and substrate-guided waves," in *Design and Manufacturing of WDM Devices*, R. T. Chen and L. S. Lome, eds., Proc. SPIE **3234,** 136–139 (1997).

22. T. K. Gaylord and M. G. Moharam, "Analysis and applications of optical diffraction by gratings," Proc. IEEE, **73,** 894–937 (1985).

23. H. Kogelnik, "Coupled wave theory for thick hologram gratings," Bell Syst. Tech. J. **48,** 2909–2947 (1969).

24. C. B. Burckhardt, "Diffraction of plane wave at a sinusoidally stratified dielectric grating," J. Opt. Soc. Am. **56,** 1502–1509 (1966).

25. J. E. Ludman, "Approximate bandwidth and the diffraction efficiency in thick holograms," Am. J. Phys. **50,** 244–246 (1982).

26. W. J. Gambogi, A. M. Weber, and T. J. Trout, "Advances and applications of DuPont holographic photopolymers," in *Holographic Imaging and Materials*, T. H. Jeong, ed., Proc. SPIE **2043,** 2–13 (1993).

27. W. J. Gambogi, W. A. Gerstadt, S. R. Mackara, and A. W. Weber, "Holographic transmission elements using improved photopolymer films," in *Computer and Optically Generated Holographic Optics: IV*, I. Cindrich and S. H. Lee, eds., Proc. SPIE **1555,** 256–267 (1991).

28. W. J. Gambogi, K. Steijin, S. Mackara, T. Duzick, B. Hamzavy, and J. Kelly, "HOE imaging in DuPont holographic photopolymers," in *Diffractive and Holographic Optics Technology*, I. Cindrich and S. H. Lee, eds., Proc. SPIE **2152,** 282–293 (1998).

29. T. H. Jamieson, "Thermal effects in optical systems," Opt. Eng. **20,** 156–160 (1981).

30. S. X. Wu, C. S. Cheng, T. Huang, S. Qin, J. Yeh, Q. Gao, A. Chen, C. P. Yeh, A. Harton, and K. Wyatt, "An experimental study on mechanical, thermomechanical, and optomechanical behaviors of holographic materials," in *Holographic Materials IV*, T. J. Trout, ed., Proc. SPIE **3294,** 145–151 (1998).

31. C. Zhao, J. Liu, Z. Fu, and R. T. Chen, "Shrinkage-corrected volume holograms based on photopolymeric phase media for surface-normal optical interconnects," Appl. Phys. Lett. **71,** 1464–1466 (1997).

32. R. A. Orwoll, "Densities, coefficients of thermal expansion, and compressibilities of amorphous polymers," in *Physical Properties of Polymers Handbook*, J. E. Mark, ed. (American Institute of Physics, Woodbury, N.Y., 1996).

33. J. Yeh, A. Harton, and K. Wyatt, "Realibility study of holographic optical elements made with DuPont photopolymer," Appl. Opt. **37,** 6270–6274 (1998).

34. Corning InfiniCor 50-μm-core multimode fibers.

35. D. R. Lide, ed., *CRC Handbook of Chemistry and Physics*, 79th ed. (CRC, Washington, D.C., 1999).